Numerical simulation of a single-element GOx/GCH_4 rocket combustion chamber using a non-adiabatic flamelet/progress variable approach

By J. Zips, H. Müller, G. Frank AND M. Pfitzner

Institute for Thermodynamics, Universität der Bundeswehr München
Werner-Heisenberg-Weg 39, 85577 Neubiberg

Inspired by earlier workshops on Rocket Combustion Modeling, the SFB-TR40 summer programm 2015 organising commitee invited international groups from research and industry to employ their numerical methods onto a subscale GOx/GCH_4 single element test case. This paper presents the contribution of the Thermodynamics Institute at the Bundeswehr university Munich. The test case is simulated using both unsteady RANS and Large Eddy Simulation in conjunction with tabulated chemistry. A non-adiabatic flamelet/progress variable method is applied in order to account for heat loss effects on chemical reactions. The flame structure and the flow field are examined and compared with the available experimental data.

1. Introduction

Cryogenic propellant combinations such as liquid oxygen/liquid hydrogen (LOx/LH_2) or storable propellants like MMH/NTO are used in many of today's high performance liquid propellant rocket engines (LRE). Since storable propellants are highly toxic and carcinogenic, handling and operating cost account for a significant share of the total cost and tend to become intolerable, especially in the view of new environmental regulations. Although LOx/LH_2 offers high specific impulse, the density of hydrogen is low and thereby causes a disadvantageous thrust-to-weight ratio. Moreover, LH_2 requires larger tanks due to additional effort in terms of insulation, which is further reducing its potential from a financial point of view [1]. Therefore, hydrocarbon fuels attract increasing attention in the development of future launchers as they offer lower cost, simpler handling, less pollution and comparable performance. Especially oxygen/methane (O_2/CH_4) is a promising propellant combination: high specific impulse, favorable cooling properties, high density at common tank pressures,low pollution and low cost both in production and handling are methane's interesting key characteristics for its application as LRE fuel [2, 3]. In contrast to LOx/LH_2 engines, where broad experience has been gathered in Europe, the knowledge about O_2/CH_4 combustion at relevant chamber pressures, heat transfer characteristics and injector design is still limited. Computational Fluid Dynamics (CFD) may support the development of future hydrocarbon rocket combustion chambers, reduce the cost of expensive ground testing and allow for an extensive investigation of the design space [4]. However, the intense coupling between chemistry

and fluid dynamics, the high heat release and the large number of involved species and reactions make flow field predictions challenging.

Within the SFB-TR40 summer program 2015, several groups have applied their numerical methods to a subscale coaxial single element GOx/GCH_4 combustion chamber that has been studied experimentally at the Flight Propulsion Institute at the technical university Munich [5]. By comparing various simulation approaches, discussing the validity of different models and analyzing the numerical results with respect to experimental data, the aim of the workshop was to create a better understanding of the complex physics involved in rocket combustion for all the participants. The Thermodynamics Institute at the Bundeswehr university Munich contributes with unsteady RANS (URANS) and Large Eddy Simulation (LES). LES is a promising tool to reduce the dependency of computational predictions upon empirical parameters such as Pr_t and Sc_t and to gain deeper insight in the flow physics especially when the temporal evolution is of interest. Its drawback is the high computational cost. Performing LES of industrially relevant applications using complex chemistry mechanisms is currently not feasible. We therefore use a tabulated chemistry approach to cut the computational cost taking into account heat losses at the wall. Heat losses in this region may slow down the chemical reactions, eventually quenching the flame. The flame temperature drops and reactions with low activation energy become dominant - an effect that needs to be taken into account to correctly predict the heat load on the wall. The method originates from previous work of an adiabatic flamelet solver† by Müller *et al.* [6, 7],which has been expanded by a non-adiabatic formulation by Frank *et al.* [8]. Pohl *et al.* implemented and examined an adiabatic Flamelet Generated Manifold (FGM) combustion model [9]. In the present study, the flamelet/progress variable model is extended by an additional enthalpy coordinate in order to include wall heat loss effects as described in Sec. 2. The computational method is described in Sec. 3. Sec. 4 summarizes both the test case and the numerical setups. The results are shown in Sec. 5.

2. Combustion model

Within this work a non-adiabatic flamelet/progress variable method is employed to model turbulent combustion including heat loss effects. In the flamelet concept, the turbulent flame is assumed to consist of small laminar diffusion flames, called flamelets [10]. This assumption is justified for sufficiently high Damköhler numbers, meaning that chemical time scales are small compared to convective time scales. Moreover, chemical reactions are assumed to occur in thin reaction layers that are small compared to the turbulent length scales. The local flame structure can hence be calculated in a preprocessing step using finite-rate chemistry, stored in a flamelet library and coupled to the turbulent flow using few parameters. During run-time, equations are solved for those controlling parameters and the corresponding thermodynamic quantities and species mass fractions are retrieved from the library.

2.1. *Non-adiabatic flamelet generation*

In the present study, the flamelet library is generated using laminar counterflow diffusion flames. A diffusion flame between opposed fuel and oxidizer streams can be reduced to a one-dimensional problem via coordinate transformation [10]. For unity Lewis number

† https://openfoamwiki.net/index.php/Extend-bazaar/solvers/combustion/flameletFoam

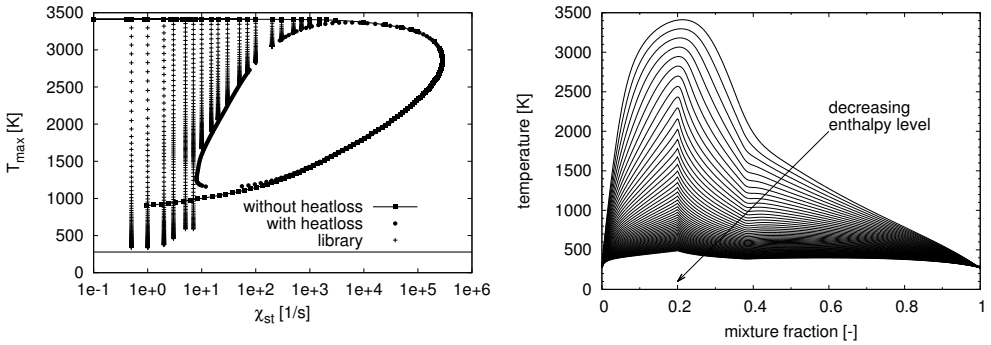

(a) Flamelet solutions. (b) Non-adiabatic flamelets for $\chi_{st} = 0.01\ s^{-1}$.

FIGURE 1. Solutions of the steady and unsteady flamelet equations with and without convective heat loss terms. For respective values of χ_{st} a certain number of flamelets is stored for decreasing enthalpy levels.

the adiabatic flamelet equations in mixture fraction space can be written as

$$\rho\frac{\partial Y_k}{\partial t} - \frac{\rho\chi}{2}\frac{\partial^2 Y_k}{\partial f^2} = \dot{\omega}_k, \tag{2.1}$$

$$\rho\frac{\partial T}{\partial t} - \frac{\rho\chi}{2}\left(\frac{\partial^2 T}{\partial f^2} + \frac{1}{c_p}\frac{\partial c_p}{\partial f}\frac{\partial T}{\partial f}\right) + \frac{1}{c_p}\sum_{k=1}^{n} h_k\dot{\omega}_k = 0, \tag{2.2}$$

with mixture fraction f, density ρ, species mass fractions Y_k and temperature T. c_p is the specific heat capacity at constant pressure, h_k is the specific enthalpy of species k and χ is the scalar dissipation rate. Chemical source terms, denoted $\dot{\omega}_k$, are computed using the GRI3.0 methane mechanism.

In order to account for wall heat loss effects in the flamelet context, Frank *et al.* [11] compared different approaches. Following their recommendation, we add a convective heat loss term on the right hand side of Eq. (2.2) as proposed by Lee *et al.* [12]. The sink term is given by

$$\dot{q}_c = -\alpha_c\left(T - T_{min}\right), \tag{2.3}$$

where T is the local temperature, T_{min} is a predefined minimum temperature within the system and α_c is a constant that is set to $\alpha_c = 5 \times 10^6\,\mathrm{kg\,m^{-3}\,s^{-1}}$. Starting from the adiabatic solution, transient flamelet solutions with sink term are stored. The operating conditions such as fuel and oxidizer temperature and pressure need to be chosen according to the boundary conditions of the test case that is to be simulated. For the present configuration, the setup is discussed in Sec. 4. The flamelet equations are solved using the FlameMaster software [13] and the solutions are stored in a database. Fig. 1(a) illustrates the results denoted by the maximum temperature of each flamelet as function of scalar dissipation rate including adiabatic steady-state solutions, non-adiabatic steady-state solutions and non-adiabatic transient solutions. It can be seen that heat loss effects significantly influence the laminar flame structure for low scalar dissipation rates and become less important for larger dissipation rates. Temperature profiles as function of mixture fraction at a specific stoichiometric scalar dissipation rate $\chi_{st} = 0.01\,\mathrm{s^{-1}}$ for decreasing enthalpy levels are shown in Fig. 1(b).

2.2. *Parametrization*

In order to use the library in CFD simulations, it is advantageous to parametrize the tables in order to obtain well-defined boundaries. Appropriate transformations for the parameters of interest, i.e., mixture fraction, mixture fraction variance, enthalpy and progress variable are presented in the following:

Mixture fraction: f is chosen as control variable. By definition $f \in [0, 1]$ and can thus be directly used for parametrization.

Progress variable: Since the steady laminar flamelet model as originally proposed by Peters [14] cannot predict flame lift-off, local extinction and re-ignition effects, an additional parameterizing quantity, called reaction progress variable $\mathcal{Y}$ is introduced [15]. Several possibilities have been suggested to define the progress variable. Here we use a linear combination of species mass fractions

$$\mathcal{Y} = \frac{Y_{CO_2}}{W_{CO_2}} + \frac{Y_{H_2}}{W_{H_2}} + \frac{Y_{H_2O}}{W_{H_2O}}, \tag{2.4}$$

where W_i are the respective molecular weights. Additionally, the progress variable is normalized with its maximum value as function of f resulting in the normalized value $\Upsilon = \mathcal{Y}/\mathcal{Y}_{max}(f) \in [0, 1]$ in order to simplify the look-up process during runtime.

Enthalpy: The total enthalpy is included as control variable in order to take into account heat loss effects. For convenience, a normalized enthalpy variable Ξ is introduced following Kim *et al.* [16] as

$$\Xi = \frac{h - h_{min}(f)}{h_{max}(f) - h_{min}(f)}, \tag{2.5}$$

with $h_{max}(f) = h_{ad}(f)$ from the adiabatic solution, since there is no significant heat gain effect in the present rocket combustion chamber test case. $h_{min}(f)$ needs to be chosen such that h_{max} and h_{min} enclose all occurring enthalpy levels. Here, the mixture fraction-dependent curve

$$h_{min}(f) = h_{ad}(f) - [h_{ad}(f_{st}) - h_{min,st}]\, g(f) \tag{2.6}$$

is chosen for the minimum enthalpy limit. $h_{min,st}$ corresponds to the enthalpy at stoichiometric conditions if the mixture was instantly cooled down to the inert mixing temperature assuming frozen composition from the adiabatic solution. The function $g(f)$ provides the bell-shape and is defined as

$$g(f) = \frac{e^{-(f-f_{st})^2}/b - f_b}{1 - f_b}, \tag{2.7}$$

where $f_b = 0.2$ is a constant determining the bell-width. Prescribing the boundary conditions $g(0) = g(1) = 0$, b is given by

$$b = \begin{cases} -f_{st}^2/ln(f_b), & \text{if } f \leq f_{st}, \\ -(1 - f_{st})^2/ln(f_b), & \text{i } f > f_{st}, \end{cases} \tag{2.8}$$

where f_{st} is the stoichiometric mixture fraction. Figure 2 shows the absolute enthalpy of various flamelet solutions as function of mixture fraction as well as the normalization curves. The blue line corresponds to $h_{ad}(f)$ and the red line denotes $h_{min}(f)$. Employing the described normalization procedure yields normalized enthalpy values Ξ in the interval $\Xi \in [0, 1]$.

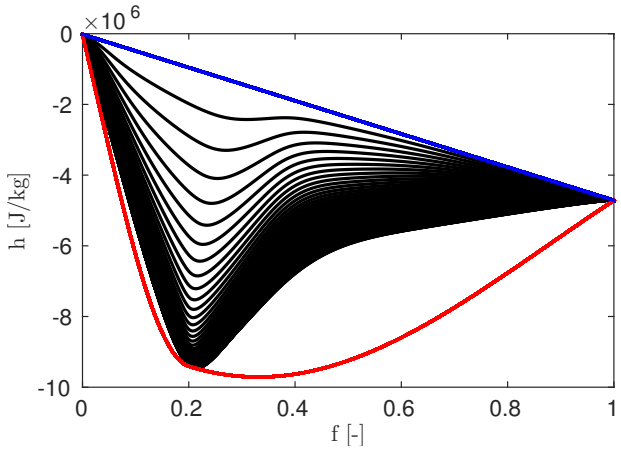

FIGURE 2. Enthalpy levels for specific scalar dissipation rate $\chi_{st} = 0.1\,\mathrm{s}^{-1}$ and values used for normalization. The blue line denotes the adiabatic solution h_{ad}, the red line represents h_{min}.

Mixture fraction variance: To account for the interaction between turbulence and chemistry on the unresolved scales, we use presumed propability density functions (PDF).

$$\widetilde{\Phi}_i = \int_0^1 \int_0^1 \int_0^1 \Phi_i \left(f, \Upsilon, \Xi\right) P df d\Upsilon d\Xi. \tag{2.9}$$

Assuming statistical independence the joint PDF P is decomposed. The shape of the PDFs for reaction progress variable and normalized enthalpy are modeled as Dirac functions. The PDF of the mixture fraction is approximated using a presumed β-PDF.

Finally, after performing the PDF integration, all mean values $\widetilde{\Phi}_i$ are stored in a multidimensional table as function of the mean values of mixture fraction $\widetilde{f}$, normalized mixture fraction variance $\widetilde{\zeta}$, normalized progress variable $\widetilde{\Upsilon}$ and normalized enthalpy $\widetilde{\Xi}$. The CFD code provides those four values, hence all required quantities can be obtained from the multidimensional table by interpolation. In the present work, the multidimensional table is resolved using an 101 x 100 x 51 x 10 ($\widetilde{f}$ x $\widetilde{\Upsilon}$ x $\widetilde{\Xi}$ x $\widetilde{\zeta}$) equidistant grid.

3. Governing equations

For the present simulations, we use the open-source software package OpenFOAM†. The publicly available code is extended to allow for simulations using the combustion model described above. The solution algorithm is based on a compressible version of the *pressure-implicit-with-splitting-of-operators* (PISO) method as proposed by Issa *et al.* [17, 18]. Instead of solving the continuity equation directly, the discretized momentum equation is used to derive a pressure evolution equation, which guarantees mass conservation. The code can be used for both RANS and LES computations. For both choices, four additional transport equations have to be solved besides the momentum and pressure equations. Note that quantities denoted as $\widetilde{\star}$ represent ensemble Favre averaged values when used in the RANS context and Favre filtered values when used in the LES context. First, the mixture fraction balance equation in cartesian coordinates

† www.openfoam.com

x_i and time t reads

$$\frac{\partial \bar{\rho}\widetilde{f}}{\partial t} + \frac{\partial \bar{\rho}\widetilde{u}_i\widetilde{f}}{\partial x_i} = \frac{\partial}{\partial x_i}\left(D_{eff}\frac{\partial \widetilde{f}}{\partial x_i}\right), \tag{3.1}$$

where u_i are the velocity components and D_{eff} is the effective mass diffusion coefficient consisting of molecular an turbulent parts. The turbulent mass diffusion coefficient is modeled by the respective turbulence model under the assumption of constant Schmidt and unity Lewis numbers. Second, the mixture fraction variance transport equation is given by

$$\frac{\partial \bar{\rho}\widetilde{f''^2}}{\partial t} + \frac{\partial \bar{\rho}\widetilde{u}_i\widetilde{f''^2}}{\partial x_i} = \frac{\partial}{\partial x_i}\left(D_{eff}\frac{\partial \widetilde{f''^2}}{\partial x_i}\right) + 2D_{eff}\left(\frac{\partial \widetilde{f}}{\partial x_i}\right)^2 - \bar{\rho}\widetilde{\chi}, \tag{3.2}$$

Third, the transport equation for the progress variable is

$$\frac{\partial \bar{\rho}\widetilde{\mathcal{Y}}}{\partial t} + \frac{\partial \bar{\rho}\widetilde{u}_i\widetilde{\mathcal{Y}}}{\partial x_i} = \frac{\partial}{\partial x_i}\left(D_{eff}\frac{\partial \widetilde{\mathcal{Y}}}{\partial x_i}\right) + \widetilde{\dot{\omega}}_{\mathcal{Y}}, \tag{3.3}$$

with the reaction progress variable source term $\widetilde{\dot{\omega}}_{\mathcal{Y}}$. $\widetilde{\dot{\omega}}_{\mathcal{Y}}$ is the sum of the source terms of the species CO_2, H_2 and H_2O and is tabulated as function of the control variables. The fourth equation is the enthalpy equation

$$\frac{\partial \bar{\rho}\widetilde{h}}{\partial t} + \frac{\partial \bar{\rho}\widetilde{u}_i\widetilde{h}}{\partial x_i} + \frac{\partial \bar{\rho}\widetilde{K}}{\partial t} + \frac{\partial \bar{\rho}\widetilde{u}_i\widetilde{K}}{\partial x_i} - \frac{\partial p}{\partial t} = \frac{\partial}{\partial x_i}\left(\alpha_{eff}\frac{\partial \widetilde{h}}{\partial x_i}\right). \tag{3.4}$$

where h is the absolute enthalpy, K the kinetic energy, p the pressure and α_{eff} the sum of molecular and turbulent thermal diffusivity. The turbulent thermal diffusivity is modeled assuming constant Prandtl number. Thus, all required variables for the look-up process are provided by the CFD solver and all quantities of interest can be interpolated from the manifold.

4. Test case and setup

4.1. *Test case*

The considered test configuration is a subscale rectangular cross-section combustion chamber with a gaseous oxygen/gaseous methane shear coaxial single-element injector. The combustion chamber extends for 290 mm and the nozzle is 20 mm long. Gaseous propellants are supplied through concentric tubes, where pure oxygen flows through the central tube and pure methane through the annulus. At the inlet, the GOx pipe diameter is 4 mm, the inner and outer GCH_4 annulus diameters are 5 mm and 6 mm, respectively. Neither oxidizer recess nor tapering are present within the configuration. The chamber cross section of 12 mm $\times$ 12 mm and the nozzle cross section of 12 mm $\times$ 4.8 mm result in a contraction ratio of 2.5. Characteristic dimensions of injector and combustion chamber are listed in Table 1. Thermocouples and pressure sensors are employed along the chamber axis and yield wall pressure distribution and transient temperature profiles. Since thermocouples are clustered with different distance to the hot wall, the assembly allows to reconstruct the wall heat flux. Detailed information concerning instrumentation, operating conditions and experimental results can be found in Celano et al. [5].

In the present test case, gaseous oxygen and methane are injected with a respective

TABLE 1. Characteristic combustion chamber and injector dimensions.

Combustion chamber			**Injector**		
Chamber length	[mm]	290	GOx diameter	[mm]	4
Chamber width	[mm]	12	GOx post wall thickness	[mm]	0.5
Chamber height	[mm]	12	GOx post recess	[mm]	0
Throat height	[mm]	4.8	GCH_4 outer diameter	[mm]	6
Contraction ratio A_{cc}/A_{th}	[-]	2.5	Injector area ratio A_{GCH4}/A_{GOx}	[-]	0.7

mass flow rate of $\dot{m}_{O2} = 0.0045\,\mathrm{kg\,s^{-1}}$ and $\dot{m}_{CH4} = 0.0017\,\mathrm{kg\,s^{-1}}$ at a temperature of $T_{O2} = 278.16\,\mathrm{K}$ and $T_{CH4} = 269.28\,\mathrm{K}$, respectively. Consequently, the operating point corresponds to a nominal chamber pressure of $20\,\mathrm{bar}$ and a nominal oxidizer-fuel ratio of $O/F = 2.6$. The hot run lasts for approximately $3\,\mathrm{s}$ in order to reach stable operation required for the thermal load measurements. Within this run time a representative time interval is chosen to evaluate and average the measured data. Wall temperature profiles have been reconstructed from the experimental results and are provided as boundary conditions. For further details concerning experimental setup and test case, the reader is referred to the official test case description [19].

4.2. *Setup URANS*

During the summer program a common setup for all groups was discussed to compare the different CFD codes used by the participating groups. Therefore, 2D URANS calculations are performed on a two dimensional grid. This grid is an axisymmetric wedge of a substitute combustion chamber with the same cross-sectional areas as the original combustion chamber. In total, the grid contains 45018 cells, with 389 cells in axial direction and 122 cells in radial direction. The injector is not included in the grid. Both post tip and methane inlet are radially resolved with 5 cells. The first cell height at the chamber wall is $0.5\,\mu\mathrm{m}$. In axial direction the grid is refined towards the faceplate. The nozzle throat is resolved with 5 cells in axial direction. Oxygen and methane are injected with a fixed massflow and uniform velocity distribution at the faceplate plane. Turbulence intensity is set to 5% at both inlets. A non-reflective pressure boundary condition is chosen at the outlet. The measured temperature profile is prescribed at the top chamber wall. The Launder-Sharma k-ε Model [20] with a turbulent Schmidt- and Prandtl number of $Sc_t = Pr_t = 0.85$ was used. Faceplate and posttip are adiabatic, no slip walls. At those two walls and the top wall in the nozzle region a wall function proposed by Launder and Spalding [21] is used.

4.3. *Setup LES*

In the LES, the computational domain encompasses the full rectangular experimental test chamber (see Fig. 3) and comprises of 20×10^6 cells; $180 \times 120 \times 931$ in the radial, circumferential and axial directions, respectively. The injector post tip is resolved using 20 cells in the radial direction and the wall distance at the non-adiabatic walls is $1\,\mu\mathrm{m}$. The injector flow is not resolved, however, realistic turbulent inflow conditions are generated by performing additional incompressible LES of the flow in the GOx pipe and the GCH_4 annulus. These simulations are carried out using cyclic boundary conditions in the axial direction. After the flow is considered fully turbulent, velocity profiles

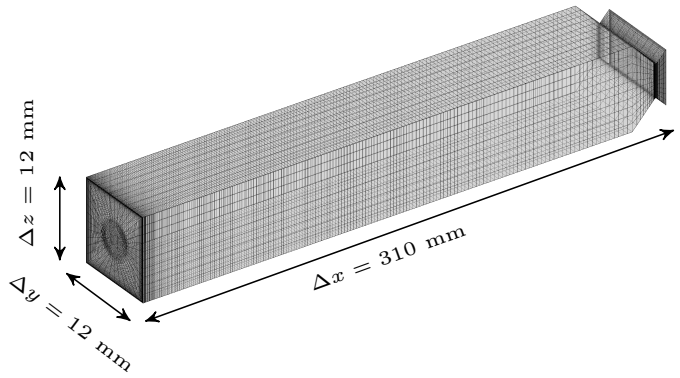

FIGURE 3. Draft of the computational domain used for the LES. Note that only every forth cell is shown and the axial extent is stretched by a factor of 0.25.

are extracted and stored in a database which is later accessed to retrieve the inflow condition for the LES of the combustion chamber. In both, the precursor simulations for the boundary condition generation and in the LES of the combustion chamber, we use the eddy-viscosity type subgrid scale (SGS) model of Vreman [22]. The SGS heat and mass flux is calculated using a constant turbulent Prandtl and Schmidt number, i.e., $Pr_{SGS} = 0.7$ and $Sc_{SGS} = 0.7$, respectively. For spatial discretization we use a second-order central differences scheme with a van Leer limiter for momentum and scalar transport to avoid unphysical oscillations. A first-order implicit Euler scheme is used for temporal discretization.

5. Results

5.1. *Flow field URANS*

A qualitative overview on the flow field and flame shape of the 2D URANS results is given in this section. The flow properties have been averaged for 10 ms. The flame in the URANS simulation is very long, as can be seen in Fig. 4. The flame is attached to the post tip. In the temperature field (bottom part) the flame thickens quickly at $x \approx 30$ mm downstream the faceplate. At the top wall a thin layer can be seen, where the hot combustion gases are cooled down to the wall temperature. In Fig. 4 HO_2 mass fraction is plotted additionally (third figure from the top), which is an indicator for the heat relase in the flame. The maximum flame temperature of around 3100 K and the maximum HO_2 mass fraction is reached far downstream close to the nozzle at $x \approx 289$ mm. The oxygen mass fraction is shown in the top part of Fig. 4. There is still unburned oxygen at the nozzle exit, meaning that the reaction is not completed at the end of the chamber. The mixing of oxygen is also quite poor and a long oxygen core is visible. Methane (second figure from the top) is trapped in the recirculation zone which is roughly 20 mm long. It is consumed quickly downstream, although near the cold wall some residual methane remains.

A close up of wall normal profiles of mixture fraction, temperature and H_2O is shown in Fig. 5 at $x \approx 200$ mm downstream the injection. A zero gradient boundary condition was used for the mixture fraction f at the wall. In the adiabatic flamelet model the same boundary condition would apply for the temperature and species fields. With the present

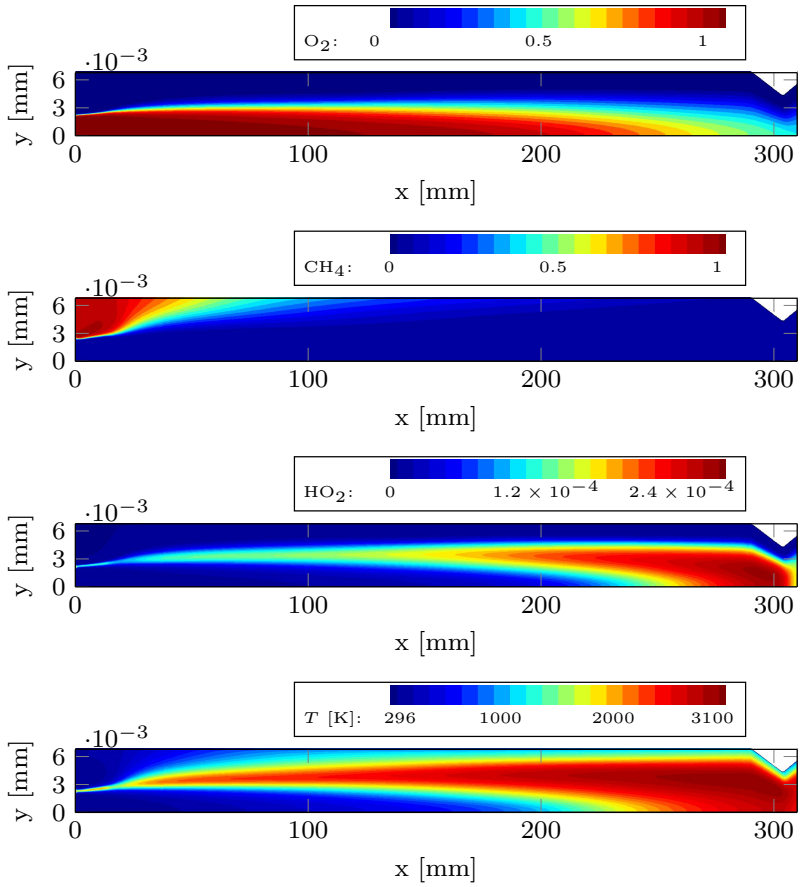

FIGURE 4. URANS: Averaged fields of O_2, CH_4 and HO_2 mass fraction and temperature. Note that the chamber is stretched by a factor of 4 in the radial direction.

non-adiabatic formulation the cooling of the fluid by the wall can be reproduced; the temperature decreases to the prescribed wall temperature. A peculiar slope can be seen in the H_2O profile. Most of the water is produced in the reaction zone in the middle of the chamber (not shown in the plot) and the mass fraction of water decreases towards the wall. But close to the wall an increase in water vapour concentration can be seen, where radicals in the cool environment recombine to stable species.

5.2. *Flow field LES*

Fig. 6 shows both instantaneous realizations (upper part) and averaged fields (lower part) of O_2 and CH_4 mass fraction as well as temperature. The instantaneous result indicates that coherent Kelvin-Helmholtz type vortices evolve close to the faceplate ($0 < x < 10$ mm). Thereafter the vortices break down and a fully turbulent flame develops. The diffusion flame that is formed between the oxidizer and fuel stream yet remains intact, i.e., no significant extinction can be observed. Comparing the LES results with the URANS fields shown in Fig. 4, it can be observed that the obtained flame shape is rather similar. Both location and absolute value of the maximum temperature is in close agreement and the downstream evolution of the averaged flame front is similar.

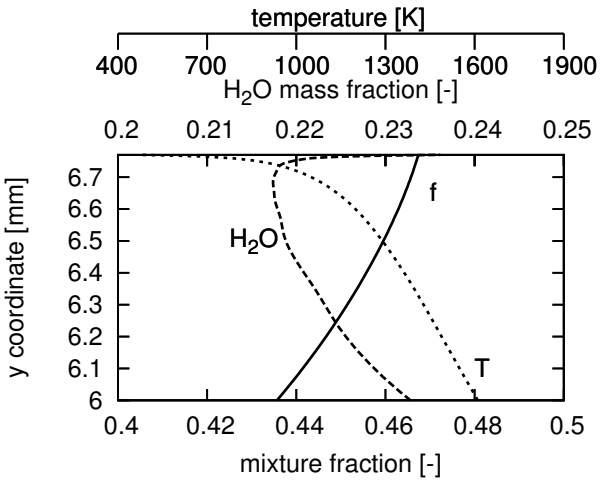

FIGURE 5. URANS: Wall normal profiles of mixture fraction, H_2O mass fraction and temperature in the near wall region at $x = 200\,\mathrm{mm}$

Differences can be observed close to the faceplate, where Kelvin-Helmholtz vortices enhance the mixing intensity in the LES and a sudden flame expansion can be observed in the averaged temperature field at $x \approx 10\,\mathrm{mm}$. This feature is not present in URANS, where a thin flame sheet with a high degree of strain can be found at this location. Furthermore, the oxygen core is longer in the URANS result and the amount of unburnt oxidizer in the nozzle thus higher.

Fig. 7 depicts the flow near the faceplate. The left plot shows the instantaneous (upper part) and averaged (lower part) temperature field together with the projected streamlines and the location of stoichiometry (white line). In the instantaneous flow field, one can observe the dominant Kelvin-Helmholtz instabilities along with the trailing recirculation zones at their tip. It is interesting to note that the radial growth rate of these instabilities determines the length of the recirculation zone in the averaged field at $x \approx 14\,\mathrm{mm}$. The radial expansion of the instability forces the trailing recirculation towards the wall. Blocking leads to a axial declaration of the recirculation zone's core and finally to stagnation. The correct numerical representation of the Kelvin-Helmholtz instabilities' downstream evolution is thus crucial to correctly predict the length of the main recirculation zone in the averaged result. Another interesting feature of the flame is the flow in the wake of the post tip, which is shown in the detailed view on the right side of Fig. 7. Two stable recirculation zones rotating in opposite directions can be observed, of which the one further downstream transports fuel towards the oxidizer stream. As a consequence, the passage is followed by a thin diffusion flame with a high degree of strain ($x > 2\,\mathrm{mm}$).

Fig. 8 shows the averaged temperature field in planes parallel to the faceplate at four axial positions. This demonstrates the downstream development of the flame, in particular, the interaction with the wall. While the flame takes the circular form that is imposed by the injector at $x = 10\,\mathrm{mm}$, the influence of the rectangular chamber can clearly be observed at $x = 50\,\mathrm{mm}$. Further downstream, at $x = 100\,\mathrm{mm}$, the flame further adapts to the chamber and at $x = 150\,\mathrm{mm}$ hot gases reach its corners. The thickness of the thermal boundary layer also adapts to the chamber geometry and is not uniform along the wall.

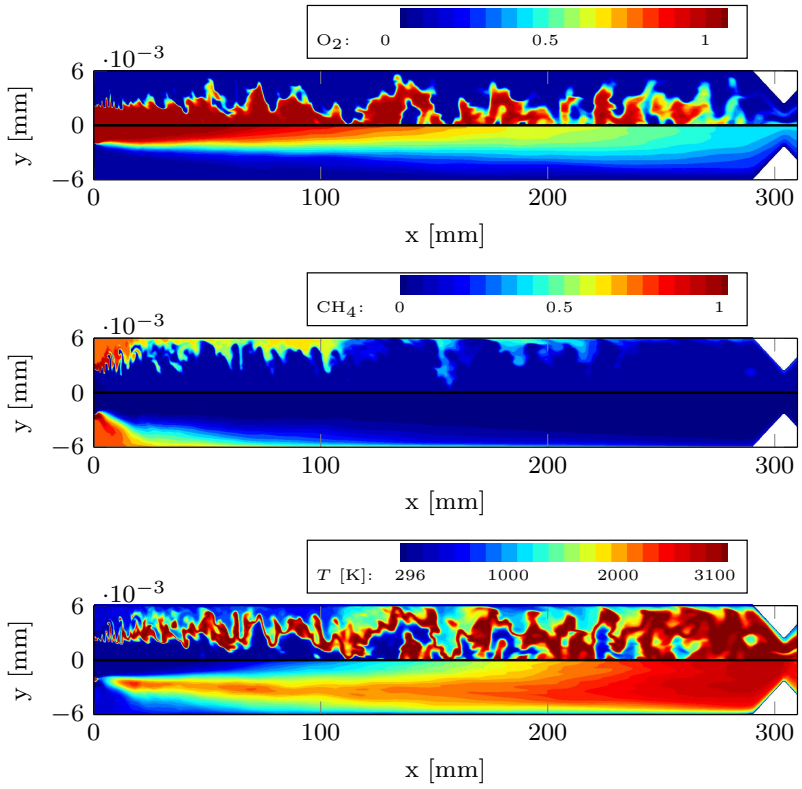

FIGURE 6. LES: Instantaneous (upper part) and averaged (lower part) fields of O_2 and CH_4 mass fraction and temperature. Note that the chamber is stretched by a factor of 4 in the radial direction.

5.3. *Comparison with experiment*

The computational result is compared to the available measurements for chamber pressure in Fig. 9. The axial profiles show that both simulations underpredict the pressure level in the chamber, with the URANS simulation being in better agreement with the measurement. The pressure level in the chamber is closely linked to the burning efficiency in the chamber, i.e., better mixing and consumption results in higher chamber pressures. This is not in line with the present simulations, where the LES result indicates less unburnt oxygen than the RANS result (see section 5.1 and 5.2) and yet predicts a lower chamber pressure. However, there are many more influencing factors such as the grid resolution in the throat, turbulence modeling and discretization, which may all contribute to the pressure level prediction and may well counteract the effect of the higher consumption rate in the LES.

The details of the axial pressure evolution can better be seen in Fig. 10, where the pressure is normalized with the value at the chamber end. After the pressure increase near the faceplate, the axial pressure gradient stays almost constant in the URANS result. This is different in the LES. The initial pressure increase is followed by a section of comparably small pressure gradient at $0.02\,\mathrm{m} < x < 0.16\,\mathrm{m}$. Thereafter the gradient increases ($0.16\,\mathrm{m} < x < 0.25\,\mathrm{m}$), indicating increased heat release. This is in line with Fig. 6, where this section corresponds to the end of the intact oxygen core. In the remaining part of the chamber ($0.25\,\mathrm{m} < x < 0.3\,\mathrm{m}$) the pressure gradient decreases again.

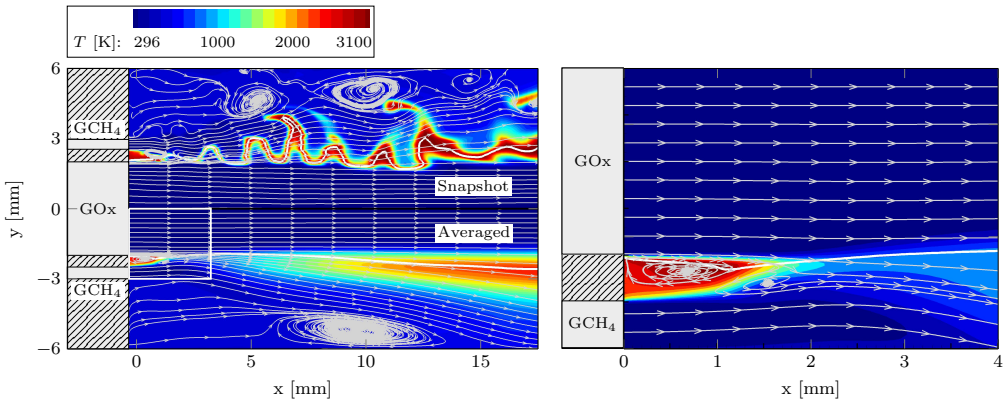

FIGURE 7. LES: Flow close to the faceplate. Left: Instantaneous (upper part) and averaged (lower part) temperature fields with projected streamlines and stoichiometric mixture line (white). Right: Detailed view of the flow in the wake of the post tip. Sector corresponds to the white box in the left plot.

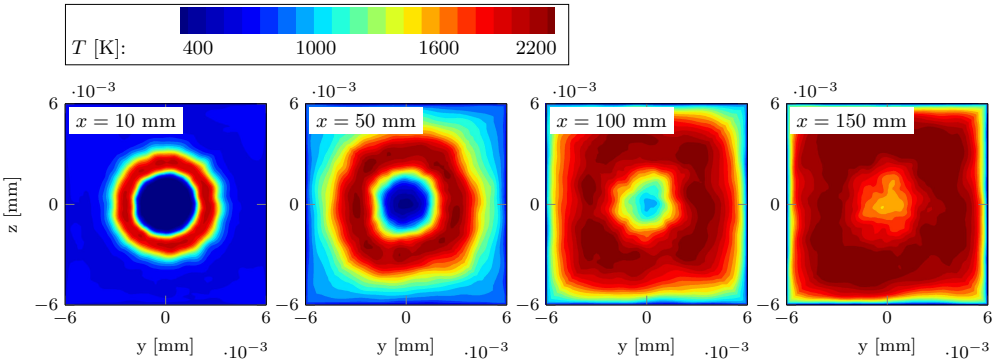

FIGURE 8. LES: Averaged temperature at four axial positions.

This alternating pattern agrees qualitatively with the experimental data even though the position of the sections is slightly shifted and the absolute pressure drop underpredicted.

6. Conclusion

Within the framework of the SFB-TR40 summer program, several groups from research and industry performed numerical simulations for a GOx/GCH_4 single element rocket combustion test case for which experimental data for wall heat flux and axial chamber pressure have been provided. In the present contribution, a tabulated chemistry approach to efficiently simulate non-adiabatic rocket combustion is presented along with computational results for the test case both in an URANS and a LES framework. The tabulation is based on non-premixed, unsteady flamelets using a complex reaction mechanism. Heat losses are represented by a sink term in the flamelet equations and the resulting manifold consequently spans a three dimensional space in terms of mixture fraction, progress variable and enthalpy level. Turbulence-chemistry interactions are taken into account with a presumed shape β-PDF.

A comparison between the URANS and the LES results shows that the averaged

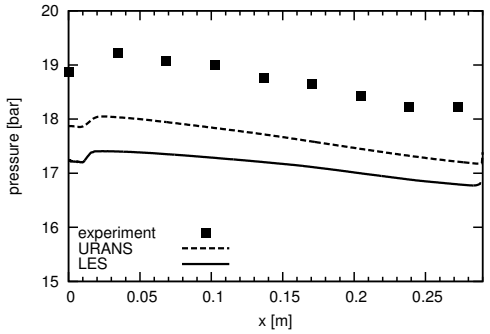

FIGURE 9. Comparison of experimental, LES and URANS chamber wall pressures

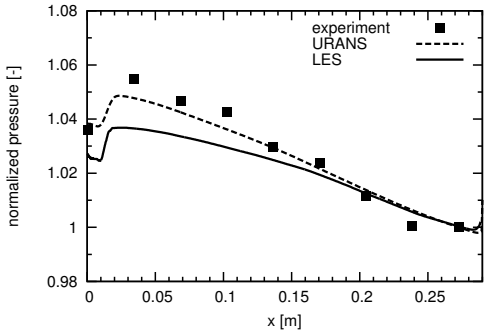

FIGURE 10. Comparison of experimental, LES and URANS normalized chamber wall pressures

flame shape is similar in both simulations. Differences could be found directly after injection, where in the LES coherent Kelvin-Helmholtz instabilities evolve and increase mixing of fuel and oxidizer. This feature is not properly reflected in the URANS. As a consequence, the oxygen core is shorter in the LES than in the URANS and the amount of unburnt oxygen in the nozzle is smaller. This is in better agreement with the experiment, where completed combustion was observed. The computational normalized axial pressure profiles are in good agreement with the experimental results, although the absolute pressure level is slightly underpredicted.

Acknowledgments

We gratefully acknowledge the German Research Foundation (Deutsche Forschungsgemeinschaft (DFG)) for providing financial support in the framework of SFB-TR 40 and the Gauss Centre for Supercomputing e.V. (www.gauss-centre.eu) for funding this project by providing computing time on the GCS Supercomputer SuperMUC at Leibniz Supercomputing Centre (LRZ, http://www.lrz.de).

References

[1] SUTTON, G. AND BIBLARZ, O. (2001). *Rocket Propulsion Elements*. John Wiley & Sons.

[2] BURKHARDT, H., SIPPEL, M., HERBERTZ, A. AND KLEVANSKI, J. (2008). Kerosene vs Methane: A Propellant Tradeoff for Reusable Liquid Booster Stages. *Journal of Spacecraft and Rockets*, **41(5)**, 762–769.

[3] PRECLIK, D., HAGEMANN, G., KNAB, O., MÄDING, C., HAESLER, D., HAIDN, O., WOSCHNAK, A. AND DEROSA, M.(2005). LOX/Hydrocarbon Preparatory Thrust Chamber Technology Activities in Germany. *41st AIAA/ASME/SAE/ASEE Joint Propulsion Conference*

[4] TUCKER, P.K., MENON, S., MERKLE, C.L., OEFELEIN, J.C. AND YANG, V.(2008). Validation of High-Fidelity CFD Simulations for Rocket Injector Design. *44th AIAA/ASME/SAE/ASEE Joint Propulsion Conference*

[5] CELANO, M.P., SILVESTRI, S., SCHLIEBEN, G., KIRCHBERGER, C. AND HAIDN O.J.(2013). Injector Characterization for a GOX-GCH4 Single Element Combustion Chamber. *5th European Conference for Aeronautics and Space Sciences (EUCASS)*

[6] MÜLLER, H., FERRARO, F. AND PFITZNER, M. (2013). Implementation of a Steady Laminar Flamelet Model for non-premixed combustion in LES and RANS simulations. 8^{th} *International OpenFOAM Workshop*, Jeju, Korea

[7] MÜLLER, H. AND PFITZNER, M. (2015). Large-Eddy Simulation of Transcritical LOX/CH4 Jet Flames. 6^{th} *European Conference for Aeronautics and Space Sciences (EUCASS)*, Krakau, Poland

[8] FRANK, G., POHL, S. AND PFITZNER, M. (2014). Heat Transfer in Reacting Cooling Films, Part II: Modelling Near-Wall Effects in Non-Premixed Combustion with OpenFOAM. *Proceedings of the ASME Turbo Expo 2014*, GT2014-25215, Düsseldorf, Germany

[9] POHL, S., MÜLLER, H. AND PFITZNER, M. (2015) Numerical simulation of turbulent non-premixed combustion using flamelet generated manifolds (FGM) in OpenFOAM. 27^{th} *Deutscher Flammentag*, Clausthal-Zellerfeld, Germany

[10] PETERS, N. (2000). *Turbulent Combustion*. Cambridge University Press.

[11] FRANK, G. AND PFITZNER, M. (2015) On the generation of non-adiabatic, non-premixed flamelet libraries with special emphasis on wall heat losses. 9^{th} *Mediterannean Combustion Symposium*, Rhodos, Greece

[12] LEE, D. J., THAKUR, S., WRIGHT, J., IHME, M. AND SHYY, W.(2011). Characterization of Flow Field Structure and Species Composition in a Shear Coaxial Rocket GH2/GO2 Injector: Modeling of Wall Heat Losses. *47th AIAA/ASME/SAE/ASEE Joint Propulsion Conference*, AIAA 2011-6125, San Diego, California

[13] PITSCH, H. (1993). *Entwicklung eines Programmpaketes zur Berechnung eindimensionaler Flammen am Beispiel einer Gegenstromdiffusionsflamme*. Diplomarbeit, RWTH Aachen.

[14] PETERS, N. (1984). Laminar diffusion flamelet models in non-premixed turbulent combustion.. *Prog. Energy Combust. Sci.*, **10**, 319–339.

[15] PIERCE, C. D. AND MOIN, P. (2004). Progress-variable approach for large eddy simulations of non-premixed turbulent combustion. *J. Fluid Mech.*, **504**, 73–97.

[16] KIM, S., JOH, M., CHOI, H. AND PARK, T. (2014). Multidisciplinary simulation of a regeneratively cooled thrust chamber of liquid rocket engine: Turbulent combustion and nozzle flow. *International Journal of Heat and Mass Transfer*, **70**, 1066–1077.

[17] R. I. ISSA (1985). Solution of the implicitly discretised fluid flow equations by operator-splitting. *J. Comp. Phys.*, **62**, 40–65.

[18] R. I. ISSA (1991). Solution of the implicitly discretised reacting flow equations by operator-splitting. *J. Comp. Phys.*, **93**, 388–410.

[19] HAIDN, O., CELANO, M.P., SILVESTRI, S., KIRCHBERGER, C. AND SCHLIEBEN, G. (2015). Test Case 1: Single Element Combustion Chamber - GCH4/GOX. *Transregio SFB-TR40 Test Case 1*.

[20] LAUNDER, B.E. AND SHARMA, B.I. (1974). Application of the Energy-Dissipation Model of Turbulence to the Calculation of Flow Near a Spinning Disc. *Letters in Heat and Mass Transfer*, **1**(2), 131–138.

[21] LAUNDER, B.E. AND SPALDING, D.B. (1974). The numerical computation of turbulent flows. *Computational Methods Appl. Mech. Eng.*, **3**, 269–289

[22] A. W. VREMAN (2004). An eddy-viscosity subgrid-scale model for turbulent shear flow: Algebraic theory and applications. *Phys. Fluids*, **16** (10), 3670–3681.